



Modelling of the degradation of martensitic stainless steels by the Boudouard reaction

Y. Gong^{a,*}, D.J. Young^b, C. Atkinson^c, T. Olszewski^d, W.J. Quadakkers^d, R.C. Reed^{a,e}

^a Department of Materials, University of Oxford, Parks Road, Oxford, OX1 3PH, UK

^b School of Materials Science & Engineering, University of New South Wales, 2052 Sydney, NSW, Australia

^c Department of Mathematics, Imperial College, London, SW7 2BZ, United Kingdom

^d Forschungszentrum Jülich GmbH, IEK-2, 52428, Jülich, Germany

^e Department of Engineering Science, University of Oxford, Parks Road, Oxford, OX1 3PJ, UK

ARTICLE INFO

Keywords:

Diffusion
CO₂ oxidation
GDOES
Boudouard reaction
Modelling

ABSTRACT

Numerical modelling of the degradation of P92 and VM12 martensitic stainless steels in gaseous (i) 70% CO₂-30%H₂O and (ii) Ar-50%CO₂ at 550 °C is reported, emphasising the formation of duplex oxide scale and internal carburisation. A 1D numerical model is presented for the evolution of multiphase regions, subject to a Robin-type boundary condition representing a Boudouard surface reaction. The surface reaction kinetics at the spinel/substrate interface and the carbon transport kinetics in the substrate result in unusual carbon concentration profiles, measured here by glow-discharge optical emission spectroscopy (GDOES). Analysis of experimental data indicates that moisture decreases the rate of the surface reaction, despite higher carbon activity of the gas.

1. Introduction

Alloy steels [1–4] and model Fe-Cr alloys [5] exposed at high temperatures to gaseous CO₂ develop oxide scales and simultaneously undergo internal carburisation. Martensitic steels (9–12 wt.% Cr) are subject to this form of attack, a matter of concern as they possess the creep strength necessary for power station service. Volume fractions of carbide precipitated can be large, reducing the ductility of the metal. Furthermore, removal of chromium from the alloy matrix (as precipitated carbide) close to the metal/scale interface ultimately renders the steel incapable of forming a protective scale. The phase transformations involved are shown schematically in Fig. 1.

Carburisation occurs despite the low carbon activity of the gas because the reacting metal is in contact with the underside of its scale, where the oxygen partial pressure, p_{O_2} , is controlled at a low value by the local equilibrium



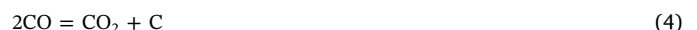
where M indicates the relevant metal. Formation of carbides beneath an oxide scale obviously means that carbon penetrates the scale. As graphite is usually not formed, carbon is assumed to be present as CO and CO₂, in proportions controlled by the equilibrium



and

$$\frac{p_{CO}}{p_{CO_2}} = \frac{K_2}{(p_{O_2}^{eq})^{1/2}} \quad (3)$$

The equilibrium carbon activity is then found from the Boudouard equilibrium which is catalysed by metal at low temperatures [6]



where underlining denotes a solute species.

Noting that CO is produced by consumption of CO₂ then the mass balance

$$p_T = p_{CO} + p_{CO_2} \quad (5)$$

is proposed, where p_T is an unknown value. It is then found [7] that the carbon activity a_C follows

$$a_C = K_4 \frac{b^2 p_T}{1 + b} \quad (6)$$

with $b = p_{CO}/p_{CO_2}$. Quantitative agreement between the a_C value calculated on the assumption $p_T = p_{CO_2}$ (gas phase) and the carbon activity corresponding to the measured amount of carbide precipitated in an Fe-9Cr model alloy exposed at 650 °C to Ar-50%CO₂ was demonstrated by Gheno et al. [7].

Given the fixed boundary condition at the scale-alloy interface resulting from its local equilibrium, it is relatively easy to solve the diffusion equations for internal carburisation, and to arrive at lifetime predictions. At lower temperatures, however, this local equilibrium

* Corresponding author.

<https://doi.org/10.1016/j.corsci.2020.108699>

Received 18 February 2020; Received in revised form 31 March 2020; Accepted 21 April 2020

Available online 16 May 2020

0010-938X/ © 2020 The Authors. Published by Elsevier Ltd. This is an open access article under the CC BY-NC-ND license (<http://creativecommons.org/licenses/by-nc-nd/4.0/>).

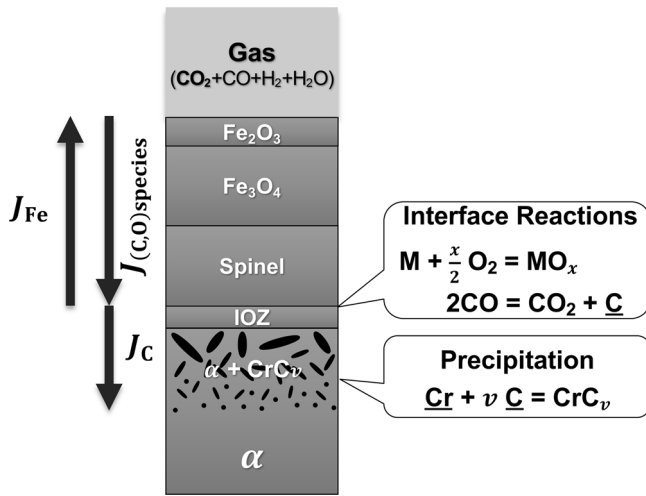


Fig. 1. Schematic illustrations of phase transformations in CO₂ oxidation of 9Cr1Mo steel. Spinel denotes a mixture of Fe₃O₄ and (Fe,Cr)₃O₄. Gas includes minority species resulting from metal oxidation reactions.

description does not hold. Boundary values for carbon concentrations at the oxide-alloy interface have been found to increase with exposure time in CO₂ at 550 °C in the 9Cr-1Mo steels T91 [8] and P92 [9], and the 12Cr steel VM12 [9]. Much longer exposures of a 9Cr-1Mo steel in pressurised CO₂ (~42bar) showed that almost 20,000 h were required to saturate a 1 mm thick sheet of steel with carbon at 600 °C [10,11]. Clearly, this slow approach to equilibrium must be explicitly taken into account in any model used for lifetime prediction.

Recognising that reaction defined in (4) is not at equilibrium, kinetic descriptions for carbon injection into the metal have been proposed [8–11]. In the simplest formulation, this rate (inward flux of carbon J_C^*) is assumed to be proportional to the difference between the actual concentration C_C^* and the corresponding equilibrium value C_C^{eq} :

$$J_C^* = \alpha(C_C^{eq} - C_C^*) \quad (7)$$

Solute carbon within the alloy then participates in two processes, inward diffusion through the metal matrix and removal from the matrix as chromium-rich carbide precipitates. The latter are immobile, interfacial effects are ignored and carbon diffusion is assumed to occur only through the ferritic matrix. In this situation, the usual diffusion equation is replaced by

$$\frac{\partial C_C^{\alpha}}{\partial t} = D \frac{\partial^2 C_C^{\alpha}}{\partial z^2} - \frac{\partial C_C^p}{\partial t} \quad (8)$$

where C_C^{α} and C_C^p are carbon concentration in matrix and carbide precipitates respectively. Solution of this equation requires specification of the relationship between C_C^{α} and C_C^p . The appropriate expression is found from the equilibrium statement for carbon between the two phases. In the case of a binary chromium carbide, this is obtained from its solubility product [9]. In the more general case of a solid solution carbide in a multi-component system, the relevant thermodynamic data must be used. The latter approach is employed here, using the thermodynamic database TCFE8 from Thermo-Calc.

The combined diffusion-precipitation equation (8) with boundary condition (7) has been solved for the one-dimensional semi-infinite case [9] and shown to describe well the increase with time of the carbon

concentration at the steel-oxide interface. More recently [10,11], a numerical solution to the two-dimensional problem represented by a thin sheet of steel near its edge has been developed and tested. The latter model was shown to reproduce accurately the evolution with time of carbon concentration profiles across the sheet. Despite these successes, significant problems remain.

The primary aim of the present work is to rigorously derive a more robust theoretical (and numerical) framework treating the kinetics of non steady-state carburisation including the kinetics of the Boudouard reaction and carbon diffusion in the ferritic matrix taking explicit account of varying precipitate volume fractions. The secondary purpose is to study the influence of gas moisture content on carbon uptake kinetics. The unexpected value of diffusion coefficient of carbon in the substrate derived from the analysis is also discussed in this paper.

2. Experimental details

For the present study two martensitic steels P92 and VM12 were used as test materials. Detailed chemical compositions are given in Table 1.

For the corrosion experiments, samples of dimension 20 × 10 × 2 mm were cut from the delivered alloy tubes. The specimens were exposed at 550 °C to flowing Ar-50%CO₂ or 70%CO₂-30%H₂O mixtures for 24, 50, 100 and 150 h [12].

Prior to the oxidation tests, the specimens were ground to a P1200 surface finish with silicon carbide paper and degreased in ethanol. The oxide scales and carbide precipitates formed during oxidation were studied by the light optical microscopy. Elemental concentration profiles across the reaction zone were measured by glow discharge optical emission spectroscopy (GDOES).

3. Experimental results

Metallographic cross-sections of the oxidation products developed during reaction with 70%CO₂-30%H₂O mixtures are shown in Figs. 2 and 3. Both steels formed an external scale of three layers: an outermost layer of Fe₂O₃, an intermediate Fe₃O₄ layer and an innermost mixed (Fe₃O₄ + (Fe,Cr)₃O₄) layer. Beneath the scale is an internal oxidation zone (IOZ). Etching the cross-sections using 25% NH₃ solution reveals heavy carburisation of both alloys beneath their oxide scales (Fig. 4).

The thickness of each oxide layer was measured and the results are summarised in Table 2. The total oxide thickness (3-layered scale plus IOZ) was measured, using the maximum in carbon concentration (see below) as a marker for the IOZ front. As seen in Fig. 5, oxidation kinetics are found to follow the parabolic law. Similar plots for individual product layers (not shown) reveal that each of the Fe₂O₃, Fe₃O₄ and spinel layers thicken according to approximately parabolic kinetics.

Reaction of the steels with Ar-50%CO₂ produced the same reaction morphologies: a triple layered external oxide scale, a shallow internal oxidation zone and a deep internal carburisation region [9]. Individual layer thicknesses measured from the relevant micrographs are also shown in Table 2. Total oxide thickness measured from the scale surface to the maximum in carbon concentration at the IOZ front are also plotted in Fig. 5.

Both steels oxidised more slowly in wet CO₂ than in dry gas. In each gas, slopes of the kinetic plots for the two steels are almost equal. However, in dry gas, the total oxide thickness for P92 is greater than for

Table 1

Composition of studied alloys (in wt.%) analysed by inductively coupled optical emission spectroscopy (ICP-OES) and infrared analysis [9].

Alloy	Cr	Ni	Mo	C	Nb	Al	W	N	V	Si	Mn	Co	Fe
P92	8.9	0.23	0.38	0.09	0.05	0.03	1.20	0.04	0.20	0.30	0.43	–	Bal.
VM12	11.4	0.20	0.27	0.11	0.05	0.02	1.50	0.04	0.22	0.44	0.17	1.50	Bal.

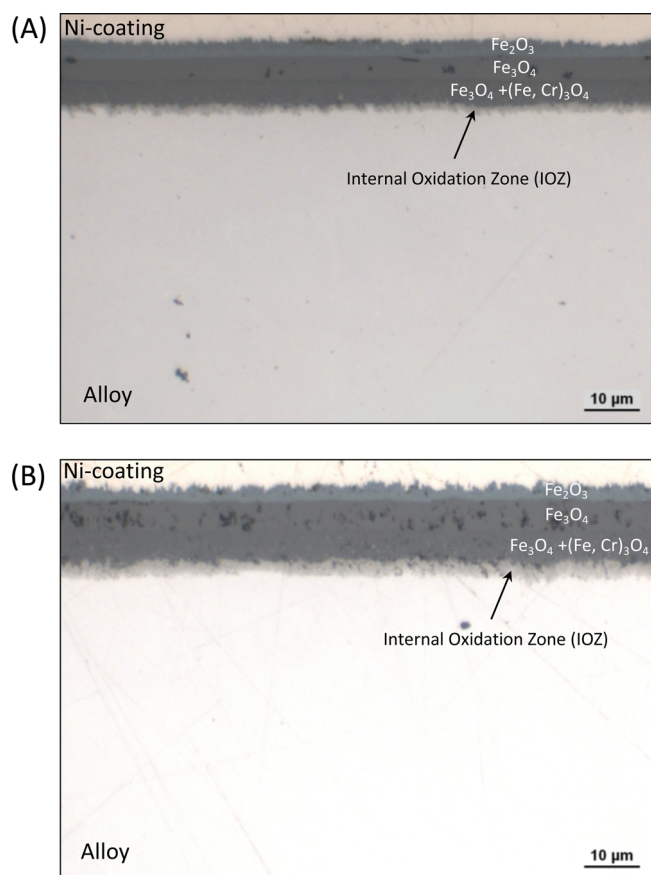


Fig. 2. Oxide scales grown on P92 steel reacted with 70%CO₂–30%H₂O for (A) 50 and (B) 150 h.

VM12, whereas in wet gas, oxide thicknesses are greater for VM12 than for P92.

Internal carburisation zones were analysed using GDOES. Carbon concentration profiles are shown in Figs. 6 and 7. As is seen, the maximum carbon concentration at the oxide-alloy interface increases with exposure time in all cases. At any given depth within the steels, the local carbon concentration also increases with reaction time. The total penetration depth also, of course, increases with time, see values summarised in Table 3.

In each gas, the carbon concentrations are greater in the higher Cr content alloy, but the penetration depths less. In each steel, for any given time, the dry gas produced higher boundary value carbon concentrations and deeper penetration depths than the wet gas.

4. Detailed description of modelling approach

During exposure to CO₂ gaseous environments, steels develop an external multilayer oxide scale consisting of outermost hematite, magnetite and innermost Cr-rich mixed spinel layers, accompanied by precipitation of Cr-rich carbides within the underlying substrate (Fig. 1). As the concentration of carbon within the steel at the steel-oxide interface continues to increase with time, this boundary is obviously not at steady-state (or equilibrium) and attention to the way it changes with time is necessary.

In this section, the kinetic model will be described in terms of the boundary condition applied at the spinel/substrate interface and the treatment of carbon diffusion in the substrate. The metal loss due to oxidation will be ignored here.

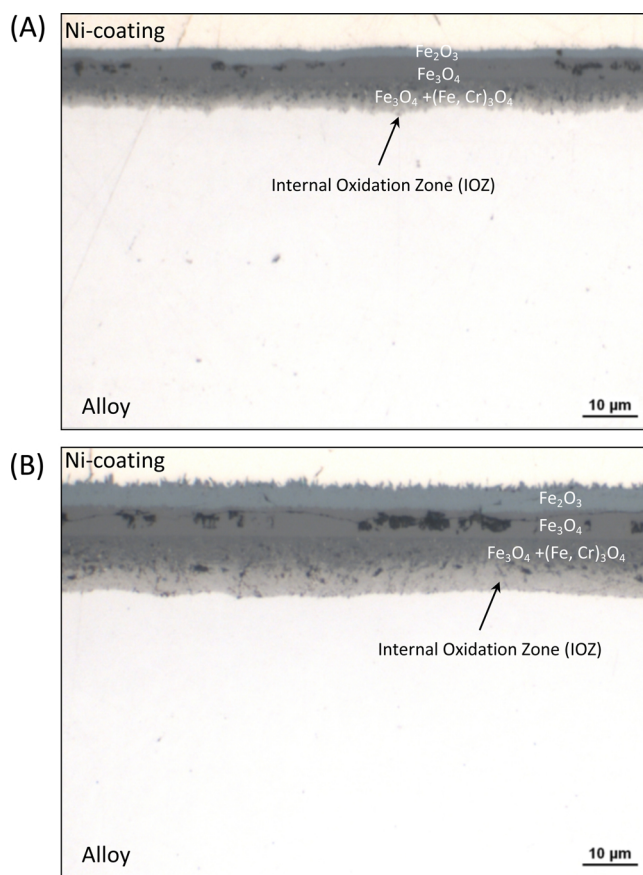


Fig. 3. Oxide scales grown on VM12 steel reacted with 70%CO₂–30%H₂O for (A) 50 and (B) 150 h.

Time integration of the system of equations which results is performed numerically, using non-linear General PDE solvers implemented in the COMSOL® v. 5.4 software package.

4.1. On the surface reaction at the spinel/substrate interface

No attempt is made here to account for the transport of carbon or oxygen [13] through the oxide scale, for which inadequate information is available. A possible mechanism involving both pore and oxide grain boundary diffusion has been proposed elsewhere [10]. Here, instead, attention is focused on the boundary conditions which apply for carbon at the spinel/substrate interface.

It is assumed [7,9] that local equilibrium among the species CO, CO₂, oxygen and carbon via Eqs. (1)–(4) is in effect within the oxide in contact with the steel. However, in the early stages of reaction, carbon activities within the steel at this interface increase with time, as shown by the increasing carbon concentrations (Figs. 6 and 7). It is concluded therefore that carbon is not equilibrated across the scale-alloy interface, but rather it is drawing nearer to local equilibrium [10,11]. The Boudouard reaction defined in Eq. (4), which produces the carbon, is extremely slow in the gas phase at this temperature, but can be catalysed at metal surfaces [14–16]. Accordingly, it is recognised that there is a kinetic impediment to carbon transfer from oxide to scale. Formally, this can be attributed to an energy barrier equivalent to an increase in carbon chemical potential, $\Delta\mu_C^b$, at the interface. A schematic energy profile for carbon near this interface is shown in Fig. 8.

The net inward diffusive flux of carbon across the spinel/substrate interface J_C^* thus can be described by:

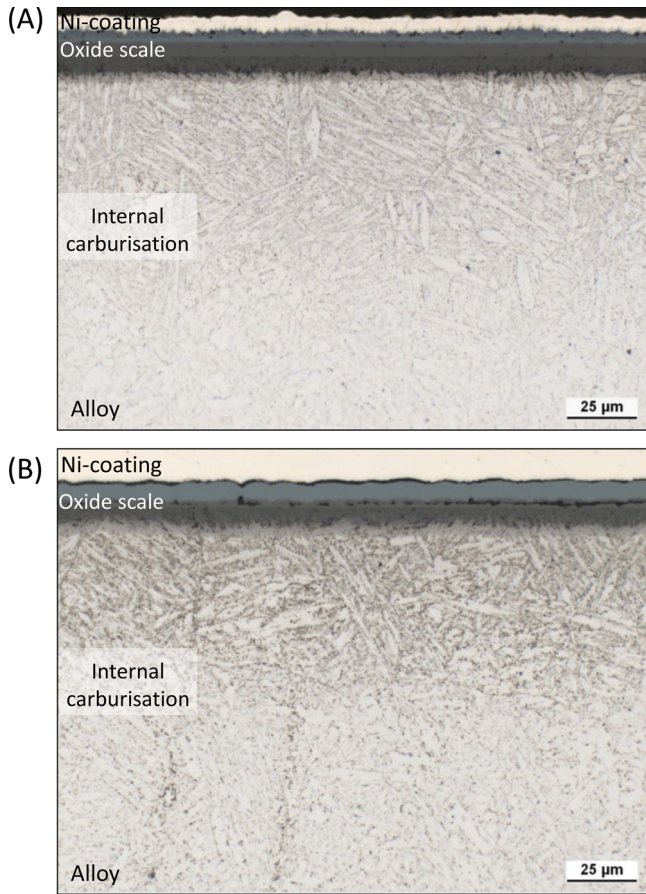


Fig. 4. Internal carburisation developed in (A) P92 and (B) VM12 alloy reacted with 70%CO₂-30%H₂O at 550 °C.

Table 2

Thickness of each oxide layer (in μm) for P92 and VM12 alloys exposed to 70%CO₂-30%H₂O or Ar-50%CO₂ gas at 550 °C.

Gas	Alloy	Oxide layer	$t = 24\text{h}$	$t = 50\text{h}$	$t = 100\text{h}$	$t = 150\text{h}$
Ar-50%CO ₂	P92	Fe ₂ O ₃	NA	4.1 ± 0.5	NA	3.2 ± 0.2
		Fe ₃ O ₄	NA	6.1 ± 0.2	NA	10.2 ± 0.6
		Spinel	NA	8.4 ± 0.3	NA	10.4 ± 0.8
		IOZ	NA	0.7 ± 0.2	NA	2.5 ± 0.3
	VM12	Fe ₂ O ₃	NA	4.5 ± 0.4	NA	8.4 ± 0.5
		Fe ₃ O ₄	NA	3.5 ± 0.4	NA	4.2 ± 0.4
		Spinel	NA	4.2 ± 0.5	NA	7.7 ± 0.6
		IOZ	NA	2.2 ± 0.4	NA	4.4 ± 0.4
70%CO ₂ -30%H ₂ O	P92	Fe ₂ O ₃	1.5 ± 0.2	2.8 ± 0.2	2.8 ± 0.3	3.6 ± 0.4
		Fe ₃ O ₄	3.7 ± 0.3	4.2 ± 0.2	5.5 ± 0.2	5.7 ± 0.2
		Spinel	2.7 ± 0.2	4.5 ± 0.2	5.4 ± 0.1	5.7 ± 0.1
		IOZ	1.6 ± 0.5	1.7 ± 0.1	2.8 ± 0.2	4.4 ± 0.2
	VM12	Fe ₂ O ₃	2.0 ± 0.2	1.8 ± 0.5	2.0 ± 0.1	4.3 ± 0.3
		Fe ₃ O ₄	2.8 ± 0.2	3.4 ± 0.5	3.6 ± 0.8	5.2 ± 0.3
		Spinel	2.5 ± 0.3	3.2 ± 0.1	3 ± 1	5.4 ± 0.6
		IOZ	1.5 ± 0.2	2.8 ± 0.5	3.5 ± 0.4	5.5 ± 0.5

$$J_C^* = J_{C,0}^* \left[\exp\left\{-\frac{\Delta\mu_C^b}{RT}\right\} - \exp\left\{-\frac{\Delta\mu_C^b + \mu_C^{\text{eq}} - \mu_C^*}{RT}\right\} \right] \quad (9)$$

where μ_C^{eq} and μ_C^* are the chemical potential of carbon at the spinel/substrate interface, at equilibrium and the actual, instantaneous value, respectively, R and T have their usual meanings, and $J_{C,0}^*$ is the conventional pre-exponential kinetic factor.

By applying:

$$\mu = \mu_0 + RT \ln\{a\} \quad (10)$$

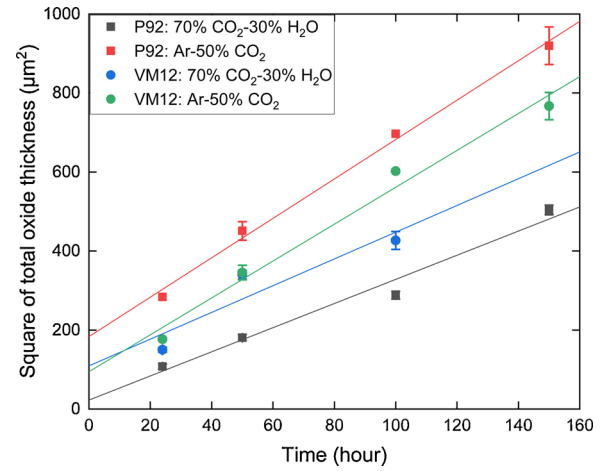


Fig. 5. Derived evolution of total oxide thickness by carbon concentration profiles measured by GDOES. Parabolic scaling kinetics are found.

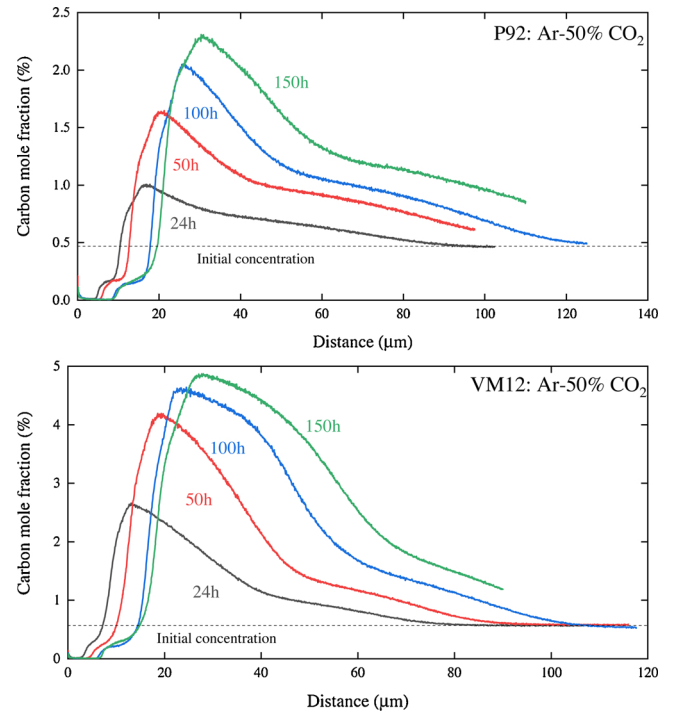


Fig. 6. In-depth carbon mole fraction profile in P92 and VM12 reacted with Ar-50%CO₂ at 550 °C, measured by GDOES, after [9].

where μ_0 is the reference chemical potential, Eq. (9) can be simplified as:

$$\begin{aligned} J_C^* &= J_{C,0}^* \exp\left\{-\frac{\Delta\mu_C^b}{RT}\right\} [1 - \exp\left\{-\frac{\mu_C^{\text{eq}} - \mu_C^*}{RT}\right\}] \\ &= J_{C,0}^* \exp\left\{-\frac{\Delta\mu_C^b}{RT}\right\} \left[1 - \frac{a_C^*}{a_C^{\text{eq}}}\right] \\ &= J_{C,0}^* \exp\left\{-\frac{\Delta\mu_C^b}{RT}\right\} \frac{1}{a_C^{\text{eq}}} (a_C^{\text{eq}} - a_C^*) \end{aligned} \quad (11)$$

where a_C^{eq} and a_C^* are the activity of carbon, at equilibrium and instantaneously at the spinel/substrate interface, respectively. The value of a_C^{eq} derived from the Boudouard reaction can be theoretically determined by the C/O gas equilibrium at the spinel/substrate interface [7].

Eq. (11) has the same form as Eq. (7), but makes explicit the role of

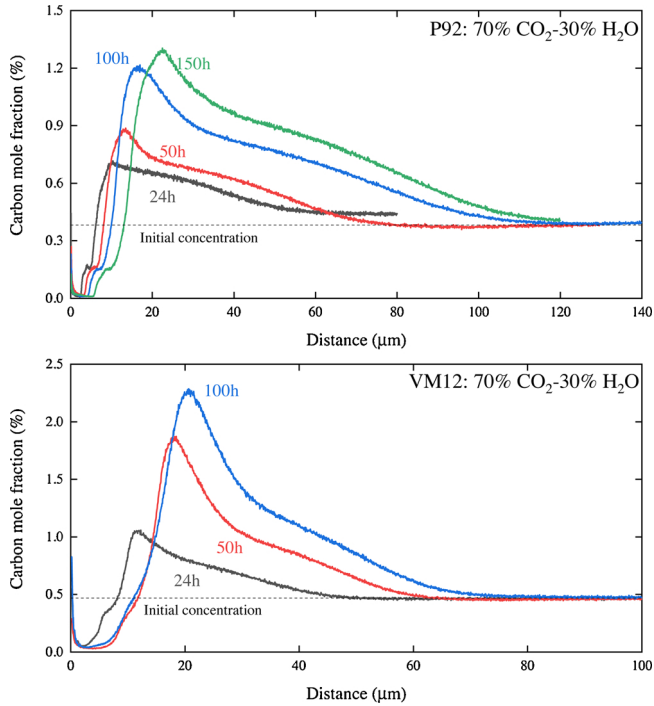


Fig. 7. In-depth carbon mole fraction profile in P92 and VM12 reacted with 70%CO₂-30%H₂O at 550 °C, measured by GDOES, after [12].

Table 3

Carburisation depth (in μm) derived from GDOES profiles as a function of time in P92 and VM12 during exposure at 550 °C in 70%CO₂-30%H₂O or Ar-50%CO₂ gas.

Gas	Alloy	t = 24 h	t = 50 h	t = 100 h	t = 150 h
Ar-50%CO ₂	P92	75	97	99	115
	VM12	64	69	81	83
70%CO ₂ -30%H ₂ O	P92	NA	61	94	99
	VM12	33	41	47	NA

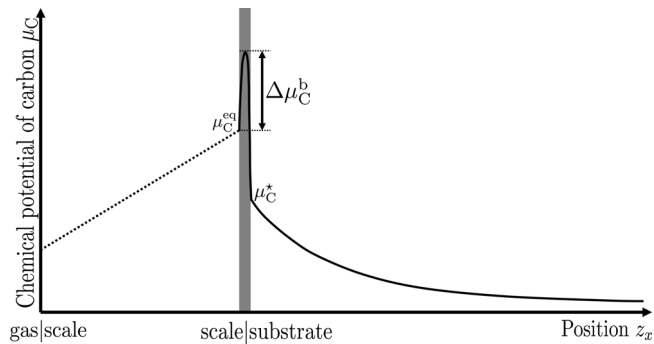


Fig. 8. Illustration of distribution of chemical potential of carbon.

the interfacial energy barrier in controlling the rate of carbon injection. The value of a_C^{eq} calculated from Eqs. (1)–(4) for the gases used here exceeds unity. [The carbon activity is predicted to be ~ 14 and ~ 366 by assuming $p_{O_2} = 2 \times 10^{-22}$ and 3×10^{-28} Pa (for a total $p_{CO_2} = 0.5$ atm) at the spinel/substrate interface, for P92 and VPM12 respectively. The carbon activity is predicted to be ~ 1.52 and ~ 1.72 at ferrite/cementite equilibrium for P92 and VPM12 respectively.] On the assumption that other processes such as graphite precipitation prevent such high values, the equilibrium carbon activity is set equal to one.

The surface reaction coefficient of carbon α_a [m·s⁻¹] is here defined as:

$$\alpha_a = J_{C,0}^* \exp\left\{-\frac{\Delta\mu_C^b}{RT}\right\} \frac{V_m}{a_C^{eq}} \quad (12)$$

where V_m is the alloy molar volume. Here α_a is taken to be alloy composition and gas chemistry specific, and also temperature dependent, i.e.

$$J_C^* V_m = \alpha_a \{T\} (a_C^{eq} - a_C^*) \quad (13)$$

4.2. On the diffusion of carbon in the substrate

Instead of solving the diffusional field of all elements in the substrate, only carbon is considered here. This is reasonable because no significant (long range) chemical inhomogeneity apart from carbon has been observed to result from either oxidation or carburisation of 9Cr steels at this temperature [9].

Because such large volumes of carbide are precipitated, it is necessary to take account of the changes in ferrite volume fraction. Fick's first law describing the carbon flux J_C in the carburised substrate can be written as:

$$J_C = J_C^\alpha + J_C^p = -f_v^\alpha D_C^\alpha \nabla C_C^\alpha - f_v^p D_C^p \nabla C_C^p \quad (14)$$

where J_C^α and J_C^p are the flux of carbon through ferrite and carbide precipitate, D_C^α and D_C^p are the chemical diffusion coefficients of carbon in ferrite and carbide precipitate respectively, f_v^α and f_v^p are the volume fraction of ferrite (the matrix) and carbide respectively, with $f_v^\alpha + f_v^p = 1$. The concentration of component i in phase k is defined as:

$$C_i^k = N_i^k / V_m^k \quad (15)$$

with N_i^k the molar fraction of component i in phase k , and V_m^k the molar volume of phase k , assuming V_m^k to be independent of minor compositional change.

In fact, Eq. (14) is valid only for prismatic shaped phases with the flux in a direction parallel to the prismatic axis. Errors arising from the application of this approximation are relatively small [17], and are ignored here. Because carbon diffuses only slowly in carbides, Eq. (14) can be approximated:

$$J_C = -f_v^\alpha D_C^\alpha \nabla C_C^\alpha \quad (16)$$

It is convenient to use the total carbon concentration $C_C = N_C / V_m$ (where N_C is the (local) total carbon mole fraction averaged over all phases in the substrate) as the state variable. The total carbon concentration is related to the local ferrite carbon concentration by equilibrium, as specified by the phase diagram. Formally, one writes

$$J_C = -f_v^\alpha D_C^\alpha \frac{dC_C^\alpha}{dC_C} \nabla C_C \quad (17)$$

This formulation has two advantages. First, it describes the distribution of total carbon, which is the quantity measured by GDOES. Second, it avoids the need to describe precipitation kinetics by incorporating an explicit statement of instantaneous local equilibrium between ferrite and carbide.

The continuity (mass balance) equation is then written in the usual form

$$\dot{C}_C + \nabla J_C = 0 \quad (18)$$

Eqs. (18) and (17) give

$$\dot{C}_C = \nabla \cdot (D_C^{\text{eff}} \nabla C_C) \quad (19)$$

where the effective diffusion coefficient of carbon D_C^{eff} is carbon concentration dependent, consistent with:

$$D_C^{\text{eff}} = f_v^\alpha D_C^\alpha \frac{dC_C^\alpha}{dC_C} \quad (20)$$

Fig. 9 shows calculated values of D_C^{eff} as a function of total mol fraction of carbon N_C at 550 °C, for P92 and VM12 alloys by assuming

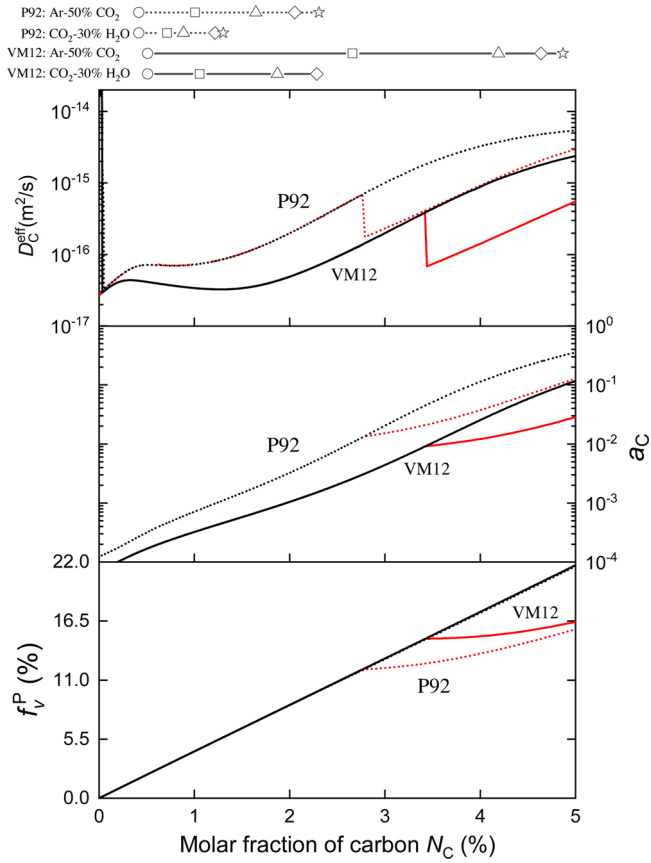


Fig. 9. Predicted effective diffusion coefficient of carbon (D_C^{eff}), carbon activity a_C (relative to graphite) and equilibrium volume fractions of carbides (f_v^P) as a function of molar fraction of carbon N_C in P92 (dot lines) and VM12 (solid lines) alloys at 550 °C; calculations were done either by only considering $M_{23}C_6$ carbide (black), or by also considering M_7C_3 carbide (red). Measured max carbon concentration by GDOES for each sample at 0 (○), 24 (□), 50 (△), 100 (◇) and 150 (☆) hours are displayed on top of the figure for comparisons.

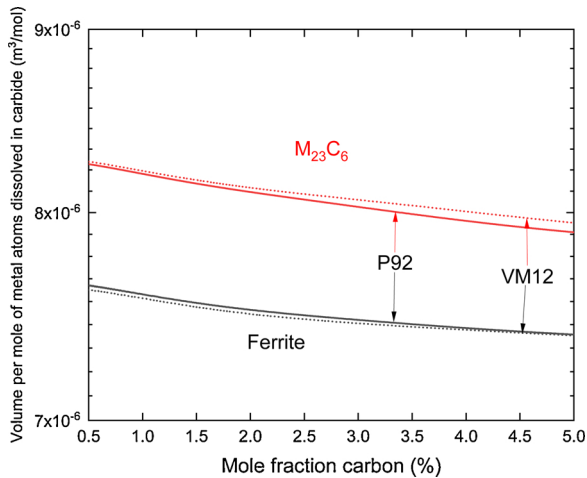


Fig. 10. Predicted volume of ferrite and $M_{23}C_6$ phases per mole of metal atoms dissolved in $M_{23}C_6$.

thermodynamic equilibrium. Values of D_C^{α} , f_v^{α} , N_C^{α} , V_m and V_m^{α} are calculated by using Thermo-Calc 2018b incorporated with the thermodynamic and molar volume assessment in the TCFe8 database and the mobility assessment in the MOBFE4 database.

In addition, carbon diffusion is related to the total carbon concentration through its effects on microstructure within the carbide

precipitation zone. Additional diffusion paths are provided by carbide/ferrite interfaces, and by dislocations within the ferrite. A correction factor, ζ , is introduced to account for these effects:

$$D_C^{\text{eff,corr}} = \zeta \{C_C\} D_C^{\text{eff}} \quad (21)$$

where ζ depends only on C_C at any given temperature. The functional form of the correction factor is not clear: whilst interfacial diffusion obviously depends on the area of precipitate-ferrite interface per unit volume, that area depends on the number density and shape of precipitates as well as C_C . As the competition between precipitate nucleation and growth changes with depth [18] the carbide-ferrite interfacial area per unit volume decreases.

The volume change accompanying precipitation is small, but significant at about 7%. The extent to which this can be accommodated likely varies with depth, and therefore C_C . Consumption of metal at the scale-alloy interface can inject vacancies into the substrate, alleviating the compressive stress due to precipitation in the subsurface alloy region [19]. Deeper within the carburised zone, this effect will not be available (carbon diffusion is much faster than ferrite lattice diffusion), and enhanced dislocation generation in the ferrite is expected to result.

In view of the difficulties in quantifying these various effects on the effective carbon diffusion coefficient, the functional form of ζ is adjusted to give the best fit to each GDOES profile.

5. Modelling results

The measured carbon profiles in Figs. 6 and 7, show total carbon concentration, C_C , i.e. the sum of the contributions from carbon solute in the ferrite and carbon contained in carbide precipitates. Their shapes are controlled by carbon injection at the scale-alloy interface (Eq. (13)), diffusion in the ferrite matrix (Eq. (16)) and local equilibrium between precipitate and matrix carbon (the derivative in Eq. (17)). Using the effective value of $D_C^{\text{eff,corr}}$ given by Eq. (21), which treats short circuit diffusion, these equations are solved by assuming a fixed position of the scale-alloy interface.

Solutions are fitted to each measured profile (in the substrate region), minimising the residuals in C_C by adjusting values of both $\zeta\{C_C\}$ and α_a . The numerical scheme for fitting is outlined in Appendix A. It should be noted that both $\zeta\{C_C\}$ and α_a are independent of t in each fitting operation for the sake of simplicity. However, different $\zeta\{C_C\}$ and α_a are found by fitting carbon distribution curves measured from samples exposed for different times.

Figs. 11 and 12 compare the resulting fitted carbon profiles with measurements. They show very good agreement. Values of α_a and ζ (averaged over C_C) emerging from this procedure are plotted in Figs. 13 and 14. It is seen that (1) both α_a and ζ vary with time, (2) the kinetic constant α_a is higher for VM12 than for P92 steel, and (3) α_a is higher for samples exposed to Ar-50%CO₂ than for those reacted with 70%CO₂-30%H₂O.

It should be emphasised that the position of the oxide/alloy interface is assumed to be fixed in these calculations. The advancing metal/scale interface can cause the pile-up of carbon at the metal/scale interface and thus accelerate the carbon ingress. The value derived for α_a thus will be decreased if metal consumption is considered.

Here a simple estimation of carbon uptake contributed by metal loss is conducted. If it is assumed that carbide precipitates are oxidised when the interface arrives, and all carbon thereby released diffuses into the metal, the mass balance for carbon rewriting from Eq. (13) then yields:

$$J_C^* V_m = \alpha_a (a_C^{\text{eq}} - a_C^*) + C_C^* V_m v^* \quad (22)$$

where C_C^* is total carbon concentration at the spinel/substrate interface and the interface moving velocity v^* can be approximated as scaling with $1/\sqrt{t}$, following the parabolic law.

By using the maximum C_C derived from each carbon profile and the

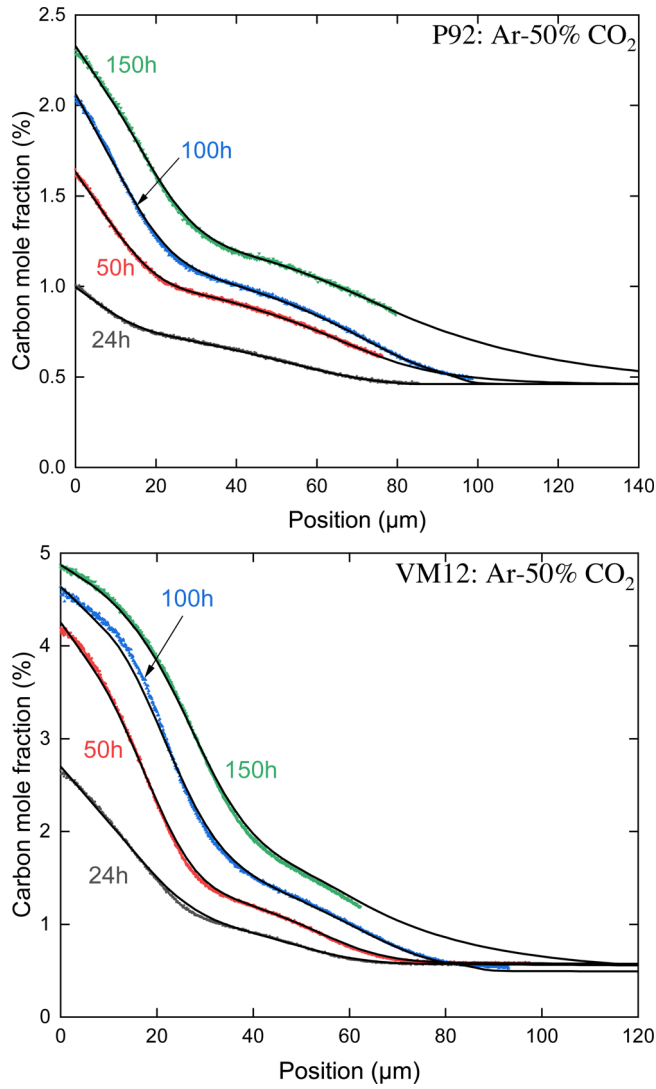


Fig. 11. Predicted carbon profile in comparison with measurements [9] for P92 alloy and VM12 alloy, exposed to Ar-50%CO₂ gas at 550 °C.

parabolic corrosion constant fitted to measured oxide thickness, the inward flux of carbon at the spinel/substrate interface due to oxidation, $N_C^* v^*$ (where N_C^* is total molar fraction of carbon at the interface), has been evaluated. Values for the four different reaction scenarios are plotted in Fig. 15 (solid lines), and compared with those contributed by the surface reaction calculated from numerical simulations (dot lines), i.e. $\alpha_a(a_C^{eq} - a_C^*)$. It is seen that the influence of metal loss due to oxidation on the surface uptake is relatively small.

6. Discussion

6.1. On the time-dependent carbon uptake kinetics

Eq. (20) describes the uncorrected effective diffusion coefficient of carbon in a volume-fixed frame of reference. The carbon concentration dependent effective diffusion coefficient evaluated in this way for P92 and VM12 is shown in Fig. 9. The maximum f_v^α value for all samples ranges from 0.84 to 0.94 (calculated from Thermo-Calc and measured carbon mole fraction, see Fig. 9) while calculated D_C^{eff} ranges from 10^{-17} to 10^{-14} m²/s. Clearly, the variation in f_v^α contributes rather little to the changes in evaluated D_C^{eff} . However, the dC_C^α/dC_C term, which relates

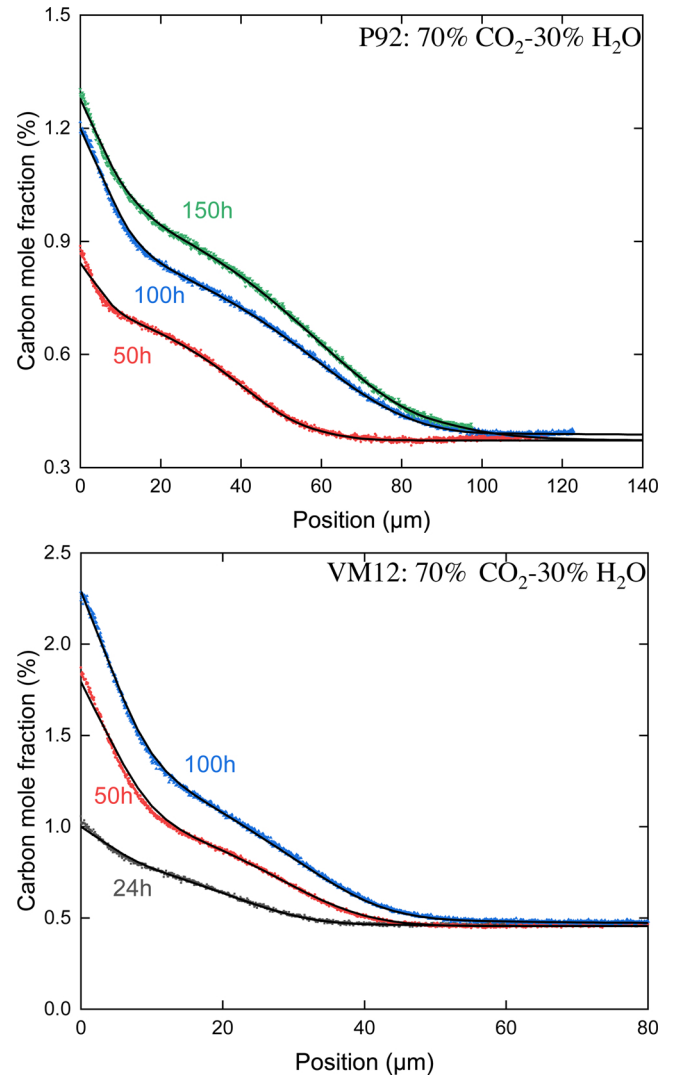


Fig. 12. Predicted carbon profile in comparison with measurements for P92 alloy and VM12 alloy, exposed to 70%CO₂-30%H₂O gas at 550 °C.

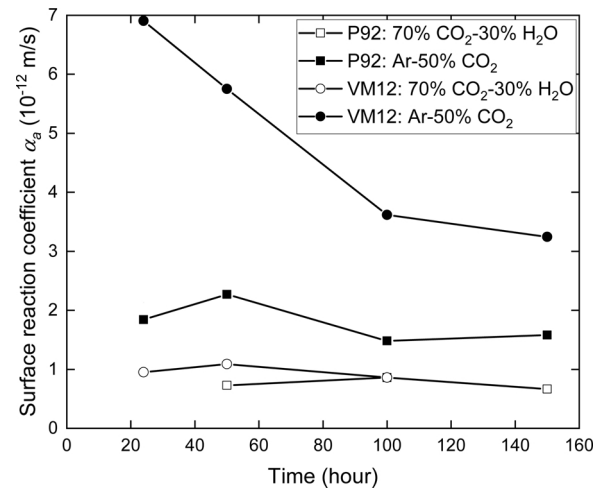


Fig. 13. Estimated surface reaction parameter α_a as a function of time, for P92 and VM12 samples exposed to Ar-50%CO₂ and 70%CO₂-30%H₂O gas at 550 °C.

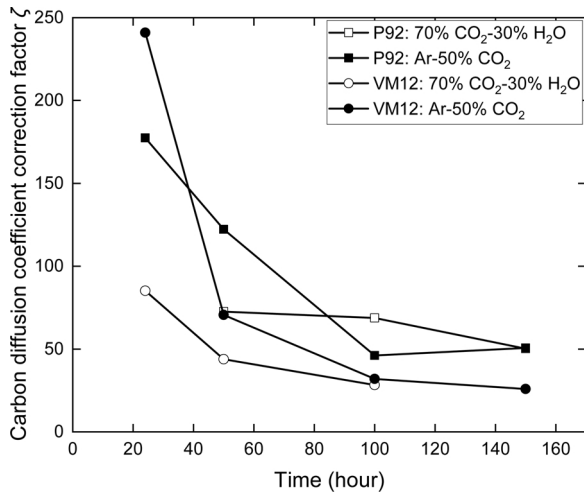


Fig. 14. Estimated carbon diffusion coefficient correction factor ζ (averaged over C_c) as a function of time, for P92 and VM12 samples exposed to Ar-50%CO₂ and 70%CO₂-30%H₂O gas at 550 °C.

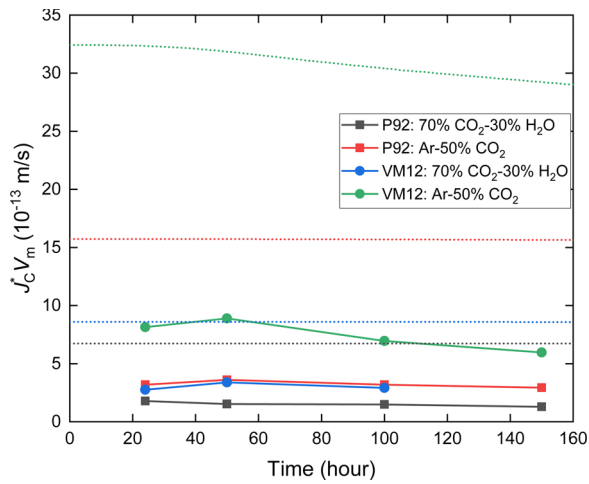


Fig. 15. Estimated inward flux of carbon at the spinel/substrate interface $J_c^* V_m$ contributed by oxidation $N_c^* v^*$ (solid lines), in comparisons with those contributed by the surface reaction $\alpha_a(a_{eq} - a_c^*)$ (dot lines).

the ferrite carbon concentration to that of carbon tied-up in carbide precipitates, shows a very strong carbon concentration dependency, varying from $\sim 10^{-5}$ at $N_c = 0.01$ to $\sim 10^{-4} - 10^{-3}$ at $N_c = 0.05$. This reflects the fact that additions of carbon to the steel are almost all precipitated as carbide. Because most carbon is in the form of compounds in which substitutional carbon diffusion is negligible, this significantly reduces D_c^{eff} values. Simplified approaches have previously been adopted [9,20] where the dC_c^z/dC_c term is approximated as composition independent, and is evaluated by averaging over the composition range.

Two different carbide precipitation zones are predicted for VM12, where M_7C_3 is predicted to be stable for $N_c \leq 3.4\%$, after exposure to Ar-50%CO₂ for 50 h and more, under local equilibrium assumptions. However no such behaviour is observed in the GDOES profiles in Fig. 6, where a discontinuity in the concentration gradient might be expected at $N_c \leq 3.4\%$. There are three reasons this discontinuity is obscured.

First, the assumption of local equilibrium at the interface between (ferrite + $M_{23}C_6$) and (ferrite + M_7C_3) zones requires instantaneous conversion of one carbide to the other as the carbon activity rises through the value corresponding to $N_c = 3.4\%$. In fact, the solid state reaction

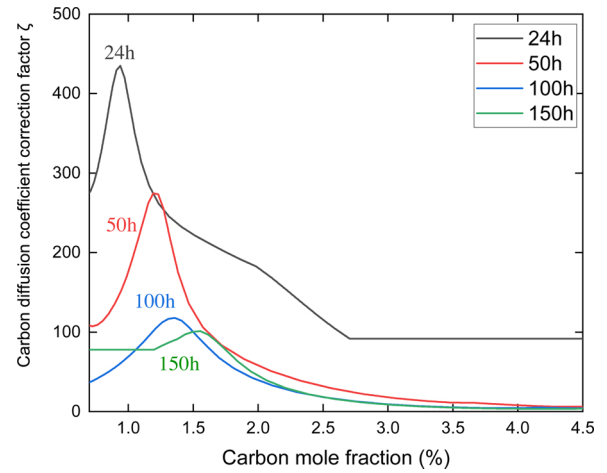


Fig. 16. Derived C_c dependent ζ for the VM12 alloy exposed to Ar-50%CO₂ at 24, 50, 100 and 150 h.

is slow, even at much higher temperatures [21,22], where a shell of the higher carbide forms around a core of the first-formed $M_{23}C_6$.

Furthermore, the carbides substitute iron for chromium to differing extents, and the two compounds co-exist in an intermediate region between M_7C_3 and $M_{23}C_6$ [22] zones.

Finally, the GDOES technique relies for its depth resolution on uniform sputtering of the composite ferrite + carbide material. Inevitably, irregularities in the bottom of the sputter crater lead to simultaneous sampling of material from different depths.

All three phenomena contribute to a spreading of the boundary between the two carbide zones, and the apparent absence of any discontinuous change between them. Nonetheless, the shape of the carbon profiles found immediately beneath the surface of VM12 after reaction for long times in dry CO₂ is different. The curves are clearly convex upwards, unlike those found in the other three reactions.

Eq. (21) takes into account the effect on the carbon diffusion coefficient of accelerated diffusion at extended defects, such as phase interfaces (e.g. ferrite/carbide interface), grain boundaries and dislocations. Estimated values of ζ (averaged over carbon concentration up to the measured maximum levels) are plotted in Fig. 14. In the cases where short-term data are available, initially high average ζ values are seen to decrease with time. Early stage values of ζ are higher in dry CO₂ reaction than in wet gas. The dependency of ζ on C_c is shown in more detail in Fig. 16, for the VM12 alloy exposed to Ar-50%CO₂. One can see that the maximum value of ζ is decreasing with time. The corresponding C_c at the location of maximum ζ , however, is increasing with time.

It is possible that the principal effect on ζ is the contribution of diffusion along precipitate-ferrite interfaces. In that case, the magnitude of the effect is related to the volume fraction of carbide (and hence C_c) but also to precipitate size, which determines the surface area to volume ratio, and precipitate shape and orientation. The last have not been characterised, and are not considered here.

The two alloys in both gases are qualitatively similar, and the example of VM12 reacted in dry CO₂ is shown in Figs. 17 and 16. As seen, in each case ζ has its maximum value at a rather low carbon content, corresponding to a region near the carbide precipitation front. It decreases from there, towards higher carbon levels, i.e. back towards the steel-oxide interface where carbon levels and carbide volume fractions are highest, see Fig. 17. It is concluded on this basis that carbide volume fraction is not the important factor determining ζ .

Precipitate size variation has not been determined, but is expected to increase with increasing depth [18], because existing precipitate growth is more favoured at lower carbon fluxes, when the supersaturation required to nucleate new ones is more slowly achieved.

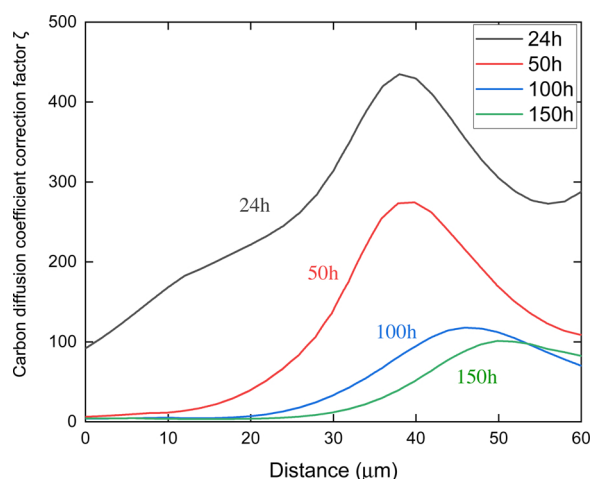


Fig. 17. Derived position dependent ζ for the VM12 alloy exposed to Ar-50%CO₂ at 24, 50, 100 and 150 h.

Larger precipitates have smaller surface area to volume ratios, and therefore provide less diffusion acceleration. It is therefore concluded that the precipitate/matrix interfacial diffusion is not the major factor accounting for variation of ζ through the carburised zone.

It is possible that dislocations generated by phase transformation strain are responsible for accelerated diffusion of carbon. This can be introduced by volume expansion during precipitation, because ferrite has a smaller molar volume (relative to metal atoms dissolved in M₂₃C₆) than M₂₃C₆ precipitates (~ 7 – 8% expansion, see predictions by Thermo-Calc in Fig. 10); a compressive stress is thus expected in ferrite matrix around precipitates. As noted in Section 4, metal consumption at the scale-alloy interface can provide space for internal carbides to form, but this effect is diminished at greater depths, where stresses are expected to be larger, and where in fact the largest increases in ζ are seen. Interface lattice misfit between ferrite and M₂₃C₆ is also expected between ferrite and M₂₃C₆ phases at different crystallographic planes [23]. This hypothesis could in principle be validated by further experiments, such as correlative electron channelling contrast imaging under controlled diffraction conditions (cECCI) and high-resolution electron backscatter diffraction (HR-EBSD) [24].

Fig. 13 plots derived values of the surface reaction rate parameter α_a . Values are approximately time-invariant in most cases, but a decrease in α_a from an initially high value is seen in the early stages of reaction for VM12 exposed to dry CO₂. As seen in the subsequent section, the faster interfacial rates evidenced by VM12 are a consequence of its chemistry. However, the explanation for the slowing of rate with time in dry CO₂ is not revealed by present results.

6.2. On the influence of moisture

When water vapour is present, the surface reaction rate constant, α_a , evaluated by fitting the carbon profiles, is significantly reduced: by up to ~ 2 times for P92 and ~ 7 for VM12 (Fig. 13). More simply, the extent of alloy carburisation is obviously reduced by the presence of water vapour (Table 3).

The presence of moisture in the gas could affect the reaction by two distinct mechanisms which have opposite effects: (1) the H₂O molecules or species derived from them can occupy oxide grain boundary sites and surface sites within the oxide pores, and perhaps on the oxide-scale interface, partially blocking CO access, and thereby slowing the C injection process. Thus selective uptake of H-bearing species decreases carbon penetration of an oxide [7]; (2) the reaction H₂O + M = H₂ + MO could facilitate the syngas reaction H₂ + CO = H₂O + C, which is usually faster than the Boudouard reaction, thus potentially accelerating the C injection.

The first possibility was suggested by Gheno et al. [7]. In that work, the estimate of carbon activity a_C at the spinel/substrate interface derived from measurements of carburisation extent and rate when H₂O was present were consistently lower than predicted from the local equilibrium model, whereas agreement was realised in the case of dry CO₂ reaction. The second possibility was the theory adopted by the early workers [25,26] on the British Magnox reactor and by those working on the advanced gas-cooled reactor (AGR). For the second possibility, considering the equilibrium of H₂O + M = H₂ + MO reaction with p_{O_2} controlled by oxidation reactions, if $p_{H_2O} + p_{H_2}$ is equal to that in the gas phase, we have $p_{H_2O}/p_{H_2} \sim 0.31$ calculated at the spinel/substrate interface for both P92 and VM12 alloys. This is significantly smaller than the value in the gas phase of 2.2×10^8 . Higher values of p_{H_2} at the spinel/substrate interface are expected to accelerate the syngas reaction H₂ + CO = H₂O + C reaction which would also inject carbon into the metal. As this does not occur, it is concluded that the syngas reaction is unimportant compared with the selective uptake of H-bearing species by the oxide, which impedes carbon penetration of the scale.

It is relevant that moisture also influences the rate of oxide scale growth. As seen in Fig. 5, scale thicknesses produced in wet gas are smaller than those grown in dry CO₂, the effect being more marked for P91 than for VM12. Scale growth is diffusion controlled, and thus the rate, for a given steel, depends only on the boundary conditions and diffusion coefficients within the oxides. Clearly, water vapour affects one or both of these. This supports the conclusion that H₂O or some species derived from it preferentially occupies oxide grain boundary and/or surface sites, thereby slowing scale growth as well as partially excluding CO₂ and/or CO.

There is a third way in which water vapour could affect carbon uptake and the rate constant α_a : interaction with the steel surface beneath the scale at positions where reaction defined in (4) is catalysed. The simplest way in which this could occur would be via preferential adsorption or reaction by H₂O, or some species derived from it, at these sites. The remaining question is why VM12 is significantly more sensitive to the water vapour effect than P91 (Fig. 13). The answer would be expected to be related to the factors contributing to the generally higher values of α_a evidenced by VM12. This steel contains cobalt, which, because of its low reactivity to oxygen, remains as finely dispersed metallic particles at and near the oxide-steel interface [9]. The resulting large metal surface area is thought to provide enhanced catalysis to the Boudouard reaction. If water vapour can interact with the cobalt surface, it is expected to affect its catalytic activity, thereby explaining the substantial decrease in α_a observed.

7. Summary and conclusions

In this paper, the corrosive attack of martensitic (9-12%Cr) stainless steels by Ar-50%CO₂ and 70%CO₂-30%H₂O at 550 °C is considered. The following specific conclusions can be drawn from this work:

- In these cases, degradation is characterised by a triple oxide scale (including an Fe-rich haematite layer, a magnetite layer and a Cr-rich spinel phase region) and the internal carburisation.
- A 1D kinetic model has been developed in this work, including the description of surface reaction (of carbon) applied at the spinel/substrate interface and the treatment of carbon diffusion in the (semi-infinite) substrate.
- The kinetics of carburisation are determined by the effective diffusion coefficient of carbon in a ferrite + carbide region, as well as a surface reaction rate parameter which characterises the sluggish Boudouard reaction at the spinel/metal interface.
- Carbon diffusion in ferrite is much too slow to support the observed rates of internal carburisation. Here, a composition-dependent correction factor $\zeta\{C_C\}$ has been introduced, which allows carbon profiles measured by GDOES to be reproduced. The physics behind

$\zeta\{C_C\}$ can be linked to the concentration of defects where the short-circuit diffusion occurs.

- $\zeta\{C_C\}$ is found to be time-dependent, with its maximum value decreasing with time, and the corresponding C_C at the maximum ζ increasing with time. This is thought to be due to changes in precipitate volume fraction and size, along with alterations in strain within ferrite induced by volume changes.
- The influence of moisture on the surface reaction kinetics is found to be more significant for the VM12 alloy than for P92.
- Surface reaction rate parameters α_a show that moisture content slows the rate of carbon uptake. Water vapour molecules, or species derived therefrom, partially block sites for carbon diffusion, and for the metal catalysed Boudouard reaction. Future work is needed to detail the mechanisms involved.

Author statement

Yilun Gong: Investigation, Methodology, Software, Writing - Original Draft Preparation

David. J. Young: Conceptualization, Supervision, Writing - Review

Appendix A. Numerical scheme of fitting

The method outlined below allows a concentration-dependent effective carbon diffusion coefficient correction factor $\zeta\{C_C\}$ to be derived from each measured carbon concentration profile.

For a 1D diffusion equation with a carbon concentration dependent diffusion coefficient $D_C^{\text{eff,corr}}\{C_C\}$:

$$\frac{\partial C_C}{\partial t} = \frac{\partial}{\partial x} \left(D_C^{\text{eff,corr}}\{C_C\} \frac{\partial C_C}{\partial x} \right) \quad (24)$$

where x is the distance. Integrating Eq. (24) with respect to x holding t constant gives [27]:

$$D_C^{\text{eff,corr}}\{C_C\{x\}\} = \frac{\int_x^\infty -\frac{\partial C_C\{x,t\}}{\partial t} \cdot dx}{\frac{\partial C_C\{x,t\}}{\partial x}} \quad (25)$$

where the $\frac{\partial C_C\{x,t\}}{\partial x}$ and $C_C\{x\}$ terms can be obtained from experiment, while the $\frac{\partial C_C\{x,t\}}{\partial t}$ term can be derived from numerical simulations with estimated $D_C^{\text{eff,corr}}\{C_C\}$ and α_a .

For each iteration, $D_C^{\text{eff,corr}}\{C_C\}$ is first calculated by using Eq. (25), and α_a is then adjusted to give the best fit to the concentration profile. Iterations stop when both $D_C^{\text{eff,corr}}\{C_C\}$ and α_a have converged.

It should be mentioned that Eq. (25) applies to any boundary conditions imposed, including the surface reaction one adopted in this paper.

References

- [1] P. Ennis, W. Quadakkers, High chromium martensitic steels - microstructure, properties and potential for further development, VGB PowerTech 81 (8) (2001) 87–90.
- [2] W. Quadakkers, J. Żurek, 1. 17 - oxidation in steam and steam/hydrogen environments, in: B. Cottis, M. Graham, R. Lindsay, S. Lyon, T. Richardson, D. Scantlebury, H. Stott (Eds.), Shreir's Corrosion, Elsevier, 2010, pp. 407–456, <https://doi.org/10.1016/B978-0-44452787-5.00022-6> ISBN 978-0-444-52787-5.
- [3] V. Lepage, G. Louis, D. Petelot, B. Lefebvre, B. Vandenberghe, Steam corrosion resistance of new 12% Cr ferritic boiler steels, Mater. Sci. Forum 461-464 (II) (2004) 1039–1046.
- [4] I. Wright, R. Dooley, A review of the oxidation behaviour of structural alloys in steam, International Materials Reviews 55 (3) (2010) 129–167, <https://doi.org/10.1179/0950666010X12646898728165>.
- [5] C.T. Fujii, R.A. Meussner, Carburization of Fe-Cr alloys during oxidation in dry carbon dioxide, J. Electrochem. Soc. 114 (5) (1967) 435, <https://doi.org/10.1149/1.2426622>.
- [6] H. Yin, J. Zhang, D.J. Young, Effect of gas composition on coking and metal dusting of 2.25Cr-1Mo steel compared with iron, Corros. Sci. 51 (12) (2009) 2983–2993, <https://doi.org/10.1016/j.corsci.2009.08.026>.
- [7] T. Gheno, D. Monceau, J. Zhang, D.J. Young, Carburisation of ferritic Fe-Cr alloys by low carbon activity gases, Corros. Sci. 53 (9) (2011) 2767–2777, <https://doi.org/10.1016/j.corsci.2011.05.013>.
- [8] F. Rouillard, G. Moine, M. Tabarant, J. Ruiz, Corrosion of 9Cr steel in CO₂ at intermediate temperature II: Mechanism of carburization, Oxid. Metals 77 (1-2) (2012) 57–70, <https://doi.org/10.1007/s11085-011-9272-4>.
- [9] D.J. Young, P. Huczowski, T. Olszewski, T. Hüttel, L. Singheiser, W. Quadakkers, Non-steady state carburisation of martensitic 9-12% Cr steels in CO₂ rich gases at 550 °C, Corros. Sci. 88 (2014) 161–169, <https://doi.org/10.1016/j.corsci.2014.07.024>.
- [10] Y. Gong, D. Young, P. Kontis, Y. Chiu, H. Larsson, A. Shin, J. Pearson, M. Moody, R. Reed, On the breakaway oxidation of Fe9Cr1Mo steel in high pressure CO₂, Acta Mater. 130 (2017) 361–374, <https://doi.org/10.1016/j.actamat.2017.02.034>.
- [11] Y. Gong, Modelling of diffusional phenomena in structural alloys for high temperature applications, (2017) Ph.D. thesis.
- [12] T. Olszewski, Oxidation mechanisms of materials for heat exchanging components in CO₂/H₂O-containing gases relevant to oxy-fuel environments, (2012) Ph.D. thesis.
- [13] H. Larsson, T. Jonsson, R. Naraghi, Y. Gong, R.C. Reed, J. Ågren, Oxidation of iron at 600 °C - experiments and simulations, Mater. Corros. 68 (2) (2017) 133–142, <https://doi.org/10.1002/maco.201508781>.
- [14] J. Gu, C.S. Hsu, L. Bai, H.M. Chen, X. Hu, Atomically dispersed Fe³⁺ sites catalyze efficient CO₂ electroreduction to CO, Science 364 (6445) (2019) 1091–1094, <https://doi.org/10.1126/science.aaw7515>.
- [15] H.B. Yang, S.F. Hung, S. Liu, K. Yuan, S. Miao, L. Zhang, X. Huang, H.Y. Wang, W. Cai, R. Chen, et al., Atomically dispersed Ni(I) as the active site for electrochemical CO₂ reduction, Nat. Energy 3 (2) (2018) 140, <https://doi.org/10.1038/s41560-017-0078-8>.
- [16] J. Schneider, H. Jia, J.T. Muckerman, E. Fujita, Thermodynamics and kinetics of CO₂, CO, and H⁺ binding to the metal centre of CO₂ reduction catalysts, Chem. Soc. Rev. 41 (2012) 2036–2051, <https://doi.org/10.1039/C1CS15278E>.
- [17] A. Engström, L. Höglund, J. Ågren, Computer simulation of diffusion in multiphase systems, Metall. Mater. Trans. A 25 (6) (1994) 1127–1134, <https://doi.org/10.1007/BF02652288>.
- [18] G. Böhm, M. Kahlweit, Über die innere Oxydation von Metallegierungen, Acta Metal. 12 (5) (1964) 641–648, [https://doi.org/10.1016/0001-6160\(64\)90036-7](https://doi.org/10.1016/0001-6160(64)90036-7).
- [19] D. Oquab, N. Xu, D. Monceau, D. Young, Subsurface microstructural changes in a cast heat resisting alloy caused by high temperature corrosion, Corros. Sci. 52 (1) (2010) 255–262, <https://doi.org/10.1016/j.corsci.2009.09.014>.
- [20] K. Nygren, Z. Yu, F. Rouillard, A. Couet, Effect of sample thickness on the oxidation and carburization kinetics of 9Cr-1Mo steel in high and atmospheric pressure CO₂ at 550 °C, Corros. Sci. (2019) 108292, <https://doi.org/10.1016/j.corsci.2019.108292>.

& Editing

Colin Atkinson: Investigation, Formal analysis

Tomasz. Olszewski: Resources

Willem. J. Quadakkers: Resources

Roger. C. Reed: Investigation, Supervision, Writing - Review & Editing

8. Data Availability

The raw data required to reproduce these findings cannot be shared at this time due to technical or time limitations.

Acknowledgement

YG and RR acknowledge financial support from EDF Energy Nuclear Generation Limited (UK) and EPSRC under grant number EP/M005607/01. The modelling approach of this paper is benefited from fruitful discussions with Prof. Alan Cocks and Prof. Simon Gill. The authors would like to thank Dr. Yuanbo Tang for the dimensional metrology.

- [21] H.J. Christ, Experimental characterization and computer-based description of the carburization behaviour of the austenitic stainless steel AISI 304L, *Materials and Corrosion* 49 (4) (1998) 258–265 doi: 10.1002/(SICI)1521-4176(199804)49:4<258::AID-MACO258>3.0.CO;2-U.
- [22] S.I. Ford, P.R. Munroe, D.J. Young, Carbonitridation of Fe-Ni-Cr alloys, in: P.F. Tortorelli, I.G. Wright, P.Y. Hou (Eds.), *John Stringer Symposium on High Temperature Corrosion*, ASM International, 2003, pp. 77–85.
- [23] A. Kipelova, A. Belyakov, R. Kaibyshev, The crystallography of $M_{23}C_6$ carbides in a martensitic 9% Cr steel after tempering, aging and creep, *Philos. Mag.* 93 (18) (2013) 2259–2268, <https://doi.org/10.1080/14786435.2013.765995>.
- [24] S. Sulzer, Z. Li, S. Zaefferer, S.M.H. Haghighat, A. Wilkinson, D. Raabe, R. Reed, On the assessment of creep damage evolution in nickel-based superalloys through correlative HR-EBSD and cECI studies, *Acta Mater.* 185 (2020) 13–27, <https://doi.org/10.1016/j.actamat.2019.07.018>.
- [25] P.C. Rowlands, J.C.P. Garrett, F.G. Hicks, S.K. Lister, B. Lloyd, J.A. Twelves, Oxidation of 9% Cr steels in high pressure high temperature CO_2 , (1974), pp. 193–207, <https://doi.org/10.1680/cosico2.00209.0020>.
- [26] P. Banks, The oxidation and carburisation of 9% Cr-1% Mo steels at temperatures between 480 and 650 °C in CO/CO_2 , (1981) Ph.D. thesis.
- [27] H. Stenlund, Three Methods for Solution of Concentration Dependent Diffusion Coefficient, (2011), <https://doi.org/10.13140/RG.2.1.5147.4006>.